Journal of Magnetic Resonance 214 (2012) 61–67

Contents lists available at SciVerse ScienceDirect

Journal of Magnetic Resonance

journal homepage: www.elsevier.com/locate/jmr

# Correcting slice selectivity in hard pulse sequences

David M. Grodzki [a,b,*], Peter M. Jakob [a], Bjoern Heismann [b,c]

[a] Department of Experimental Physics 5, University of Wuerzburg, Germany
[b] Magnetic Resonance, Siemens AG, Erlangen, Germany
[c] Friedrich-Alexander-University Erlangen-Nuremberg, Erlangen, Germany

ARTICLE INFO

*Article history:*
Received 8 August 2011
Revised 29 September 2011
Available online 13 October 2011

*Keywords:*
Non-selective excitation
Slice-selective excitation
Ultrashort echo time

ABSTRACT

Many MRI sequences use non-selective hard pulse excitation in the presence of imaging gradients. In this work, we investigate to which extent the sinc-shaped frequency excitation profiles of the pulse can be used for imaging without the generation of artefacts. A correction algorithm is proposed that eliminates the influence of the excitation profile. Phantom as well as in vivo measurements prove that enhanced image quality can be obtained as long as the first minimum of the excitation profile lies outside the imaged object.



## 1. Introduction

In Magnetic Resonance Imaging, spins are excited by slice-, slab- or non-selective sequences. For 2D imaging, shaped RF excitation pulses in combination with slice selection gradients are used to excite only one slice in the object. In 3D measurements, either a slab or the entire object is excited. Three-dimensional encoding is used to generate a 3D dataset. During a non-selective excitation, gradients are usually switched off to avoid any unwanted slice-selectivity.

A couple of sequences, like the BURST sequence [1] and sequences designed for ultrashort echo time imaging use non-selective excitations in the presence of switched-on imaging gradients. In ultrashort echo time imaging, this is motivated by the need for an immediate start of data acquisition after the pulse, as the signal of tissues with very short T2 will be decayed otherwise. Examples for these ultrashort echo time sequences are the single-point sequences RASP [2] or SPRITE [3], the radial sequences zTE [4] (initially dubbed BLAST [5]) and WASPI [6] as well as the combined radial and single-point sequence PETRA [7].

Ultrashort echo time imaging offers new applications for MRI, as short T2 tissues like bone [8], tendons [9], ligaments [10] or teeth [11] provide signal and can be evaluated. In the Ultrashort Echo Time (UTE) sequence [12], gradients are zero until the beginning of the readout. If gradients are already ramped up before the excitation, no time is lost during gradient ramping. Furthermore, no artefacts due to eddy currents during ramping and time delays of the gradient starts can occur.

In case of the zTE, WASPI or PETRA sequence, the first points of the radial half-projections are missed due to the time needed before the start of the acquisition. To recover these points in *k*-space center, zTE acquires the absolute *k*-space center with one FID and uses algebraic reconstruction algorithms [13] for other missing points. In WASPI, a few more radial spokes with lowered gradient strengths are acquired to downsize the gap in *k*-space center. PETRA fills the gap completely with single-point imaging. Without loss of generality, we will focus on the PETRA sequence in the following.

The previously mentioned sequences use a hard rectangular excitation pulse. In comparison to the hard pulse sequences, SWIFT [14] uses an excitation that is split into *n* small sub-pulses. A sub-adiabatic frequency sweep is performed over these pulses. One difference between these two excitations is the resulting spectral profile. The spectral shape of frequency swept excitations in SWIFT is a rectangular function while in hard pulse sequences the excitation profile has a sinc-shape as it is indicated in Fig. 1.

Because the imaging gradients are on during the pulse, the excitation in these sequences is not truly non-selective. A slice that is defined by the spectral profile is excited. Within the sequences, this excited slice does not only rotate while different radial projections are acquired, but also changes its thickness if the gradient strength is changed. The bandwidth of the excitation must be large enough to avoid unwanted slice-selectivity in the object. For the SWIFT sequence this means that the rectangular excitation shape must cover the entire object at the applied gradient strength. For hard pulse excitation, the full width half maximum (FWHM) should be as large as possible to ensure a homogeneous excitation. If the excitation bandwidth is not sufficient for the used gradient strength and FOV, the excitation is not homogeneous over the object, see Fig. 1.

* Corresponding author. Address: Magnetic Resonance, Siemens AG, Allee am Roethelheimpark 2, 91052 Erlangen, Germany. Fax: +49 9131 84 2186.
*E-mail address:* david.grodzki.ext@siemens.com (D.M. Grodzki).

1090-7807/$ - see front matter © 2011 Elsevier Inc. All rights reserved.
doi:10.1016/j.jmr.2011.10.005

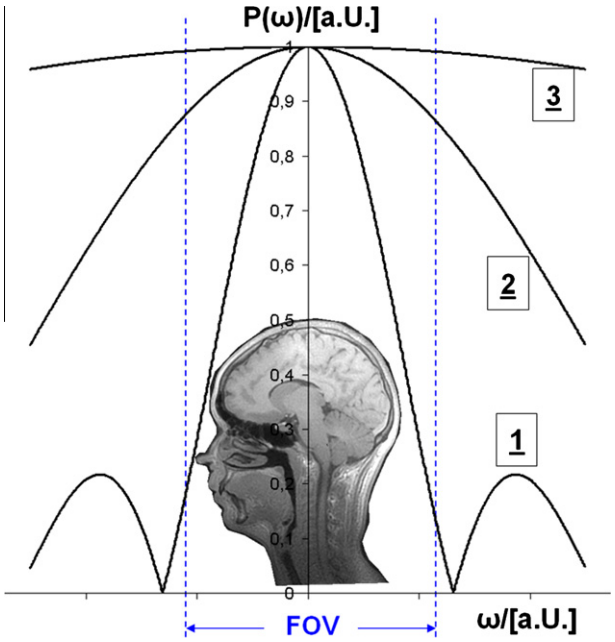


**Fig. 1.** Illustration of the unwanted slice-selectivity. If the bandwidth of the excitation is not sufficient, the excitation is not homogeneous over the object. A slice with a sinc-shaped profile is selected. The minimum of the profile within the FOV, $P_{min}$, is about 0.15 for line 1, 0.88 for line 2 and 0.98 for line 3.

The FWHM is inversely proportional to the pulse duration so that the excitation should be as short as possible. Typically, short pulses are limited to a pulse duration of a few microseconds that are needed to apply enough excitation energy for the designated flip angle. The FWHM of the sinc-shape has a typical bandwidth of 70–150 kHz on clinical scanners, e.g. 121 kHz for a 10 μs pulse, which is in the range of the excitation bandwidth during the sweep-pulsed excitation.

In this work, we investigate the influence of sinc-shaped frequency excitation profiles on the image. We assess to what extent hard pulses can be used for imaging without generating artefacts. A post-processing algorithm is presented that eliminates slice selection artefacts as long as the imaged object fits into the sphere defined by the first minimum of the excitation profile. We evaluate the performance with phantom and volunteer measurements.

## 2. Theory

Without the loss of generality, we use a one-dimensional object with the magnetization distribution $f(x)$ in image space. During an idealized MRI scan, $k$-space $F(k)$ is measured as

$$F(k) = \sum_x f(x) e^{ikx}. \tag{1}$$

To obtain an MR image, $k$-space is Fourier back transformed to image space by

$$I(x) = \sum_k F(k) e^{-ikx} \tag{2}$$

and the image $I(x) = f(x)$ is obtained.

The magnetization distribution $f(x)$ in Eq. (1) during a non-selective excitation in the presence of gradients is superposed by the spectral shape of the excitation pulse $P(\omega)$. It is given by the Fourier transformation of the pulse shape in time domain $p(t)$. The hard pulse sequences use a rectangular excitation pulse $p(t)$

$$p(t) = \begin{cases} B_1, & \text{if} |t| < \tau/2, \\ 0, & \text{elsewhere} \end{cases} \tag{3}$$

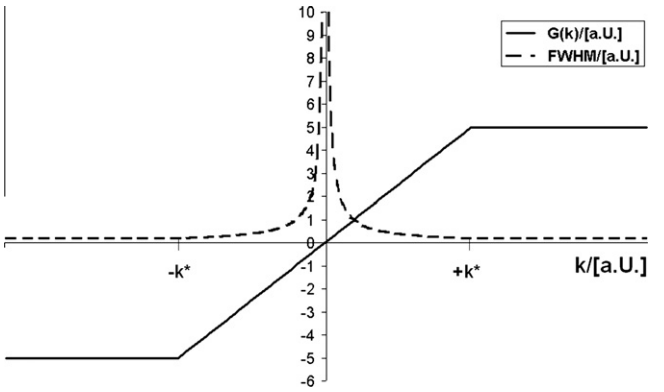


**Fig. 2.** Gradient strength of a complete line through $k$-space for the PETRA sequence. In the radial part with $|k| > k^*$, $|G|$ equals $G_{max}$. In the cartesian part with $|k| \leqslant k^*$, gradients are stepped through according to Eq. (12) for each $k$-space point. The corresponding FWHM of the excitation bandwidth (dashed line) is inversely proportional to the gradient strength. It is constant in the radial part and rises closer to the center of $k$-space in the Cartesian part.

with the duration $\tau$ and the radiofrequency (RF) excitation field $B_1$. In the frequency domain, this corresponds to a sinc-shaped spectral profile $P(\omega)$ with

$$P(\omega) = \frac{\sin\left(\frac{1}{2}\omega\tau\right)}{\frac{1}{2}\omega\tau} = \mathrm{sinc}\left(\frac{1}{2}\omega\tau\right) \tag{4}$$

and the phase factor

$$\varphi(\omega) = \exp\left(-i\frac{\omega}{2\pi}\frac{\tau}{2}\right), \tag{5}$$

which is accounted for in the $k$-space values of the reconstruction. In the presence of gradients G, the resonance frequency $\omega$ is a function of the point $x$ in image space, given by

$$\omega = 2\pi\gamma x G, \tag{6}$$

In the case of alternating gradients throughout the sequence, $\omega$ is also a function of the acquired $k$-space point $k$. The excitation profile of the pulse therefore can be expressed by $P(\omega) = P(x,k)$. The disturbed $k$-space $F'(k)$

$$F'(k) = \sum_x f(x) P(x,k) e^{ikx} \tag{7}$$

is measured. If the disturbed $k$-space $F'(k)$ is Fourier back transformed to image space using Eq. (2), the disturbed image $I'(x) \neq f(x)$ is calculated:

$$I'(x) = \sum_k F'(k) e^{-ikx}. \tag{8}$$

We propose to solve the influence of the excitation profile by using a matrix inversion instead of Fourier back transformations. Defining the matrix

$$D_{kx} = P(x,k) e^{ikx} \tag{9}$$

with $N \times N = N^2$ elements, Eq. (7) can be rewritten as a matrix equation

$$F'_k = D_{kx} \mathrm{f}_x. \tag{10}$$

$F'_k$ is the disturbed $k$-space data measured in the MRI scan. The elements of $D_{kx}$ are known and can be calculated. They depend on the gradient trajectories and timings of the specific sequence, pulse profiles, resolution and FOV. The system of linear equation in Eq. (10) can be solved by a matrix inversion

$$\mathrm{f}_x = I_x = D_{kx}^{-1} F'_k \tag{11}$$

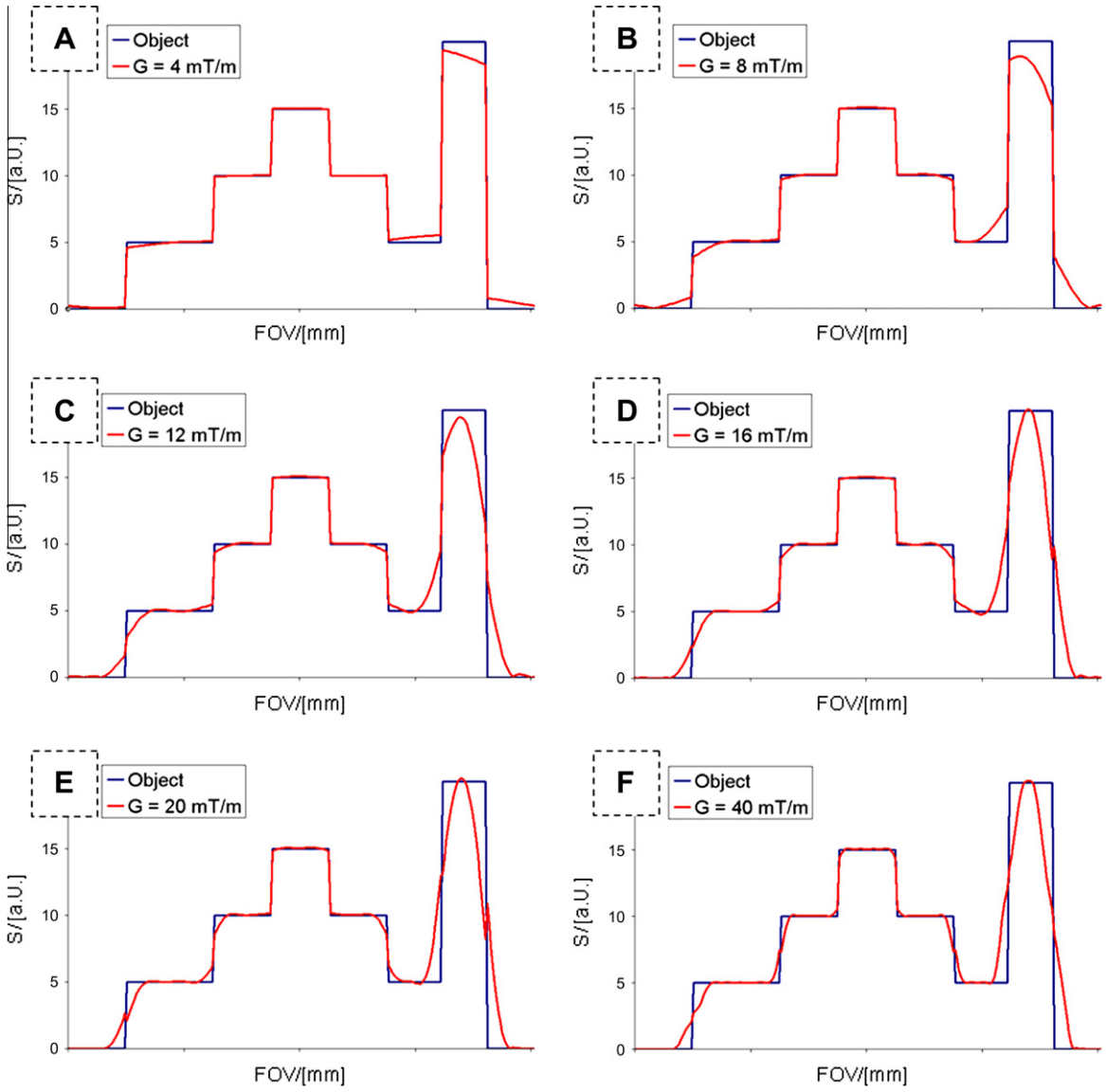


**Fig. 3.** Simulation of a one-dimensional object $f(x)$ and the expected disturbed image $I'(x)$ for different gradient strengths. The corrected images $I(x)$ (not shown) do not show any differences compared to $f(x)$. Simulated FOV = 300 mm, $N = 250$, pulse duration $\tau = 14$ μs and TE = 70 μs.

and the undisturbed image $I_x = f_x$ is obtained.

## 3. Methods

### 3.1. PETRA sequence

With non-zero imaging gradients during the excitation, a slice defined by the gradient vektor $\vec{G}$ and Eq. (4) is excited. During the radial acquisitions of the PETRA sequence, the absolute gradient strength is kept constant at $|\vec{G}| = G_{max}$. The direction of the gradient vector is altered for every repetition and radial spokes that are evenly distributed over a sphere are acquired. The excited slices rotate according to the direction of the projection.

The echo time TE is limited by the time needed for switching the coils from transmit to receive mode and the pulse duration. During this period, $k$-space points in the middle of $k$-space with $|\vec{k}| \leqslant k^* = (\gamma \text{ TE } G_{max})$ are missed, because encoding of spins starts in the middle of the pulse. To recover the missing $k$-space information in the middle of $k$-space, supplementary scanning is conducted. PETRA acquires the missing points in $k$-space center by single-point measurement, with

$$\vec{G} = \gamma\ \vec{k}/\text{TE}. \tag{12}$$

Fig. 2 illustrates the gradient strengths $G(k)$ for one projection through $k$-space for the PETRA sequence. Inserting the $k$-space depending gradient strength $\vec{G}(\vec{k})$ and Eq. (6) into Eq. (4), we obtain

$$P(\omega) = P(\vec{r}, \vec{k}) = \text{sinc}(\pi\ \gamma\tau\vec{r} \cdot \vec{G}(\vec{k})). \tag{13}$$

The FWHM of this excitation profile on a projection through $k$-space is plotted in Fig. 2 (dashed line). The FWHM indicates the thickness of the slice selected during the excitation. While the slice thickness is constant in the radial part, it rises as it comes closer to the center of $k$-space in the Cartesian part.

We define $r_0 = (\gamma\tau G_{max})^{-1}$ as the radius in image space, where the spectral profile has its first minimum using $G_{max}$. If $r_0$ is outside the FOV, $P_{min}$ is the minimal value of $P(\vec{r}, \vec{k})$ during one measurement. $P_{min}$ is reached at $|\vec{G}| = G_{max}$ and the outer edge of the FOV, where $|\vec{r}| = FOV/2$. $P_{min}$ illustrates the excitation decrease at the outer edges of the FOV, see Fig. 1. The maximum of the spectral profile is always situated in the center of the image and is normalized to one.

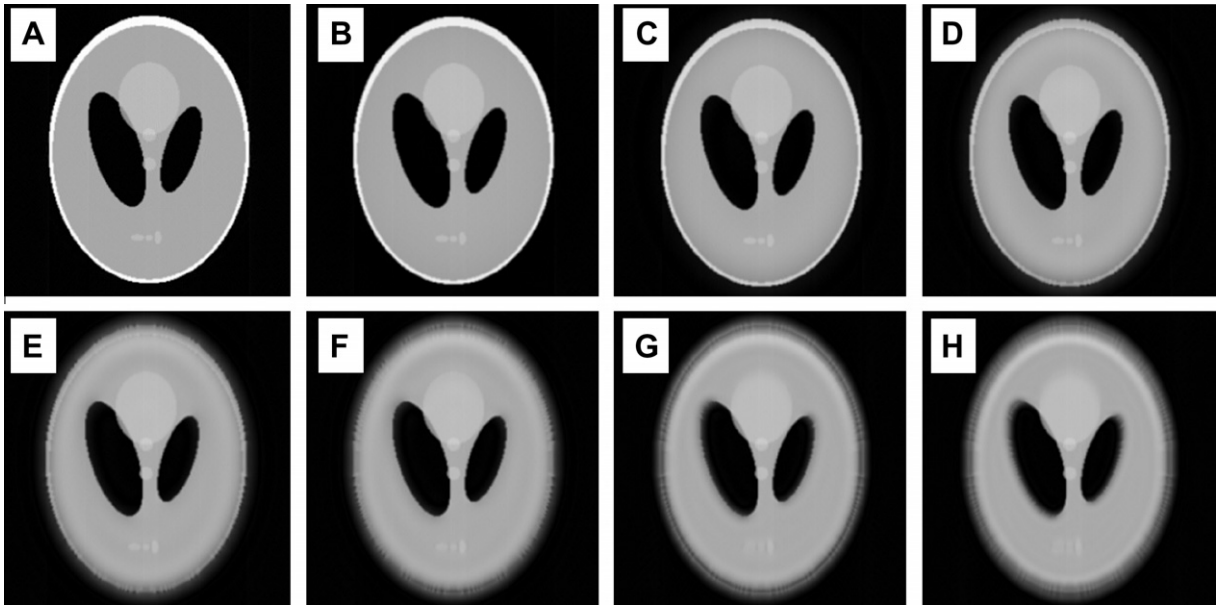


**Fig. 4.** Simulation of a two-dimensional object $f(x,y)$ and the expected disturbed image $I'(x,y)$ for different gradient strength with the original object in A. Maximum gradients strengths were 4, 8, 12, 16, 20, 30 and 40 mT/m from B to H. The corrected images $I(x,y)$ (not shown) do not show any differences compared to $f(x,y)$. Simulated FOV = 300 mm, $N = 250$, pulse duration $\tau = 14$ µs and TE = 70 µs.

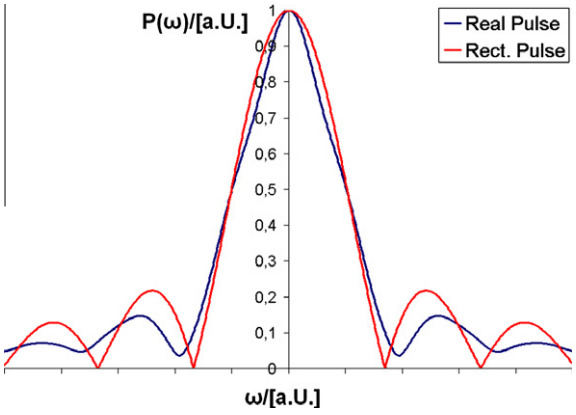


**Fig. 5.** Excitation profile of a theoretical rectangular excitation and the profile of the pulse that is actually applied by the RFPA.

$P(\vec{r},\vec{k})$ is symmetric with respect to the origin for both the point in image space $\vec{r}$ and in $k$-space $\vec{k}$ and only depends on the absolutes $|\vec{r}|$ and $|\vec{k}|$. This radial symmetry of the problem is used in the 3D data handling.

### 3.2. Image correction in 3D

The correction approach presented in the theory section can in principle also be used in higher dimensions than one. The matrix size increases from $N^2$ to $N^4$ elements in 2D and $N^6$ elements in 3D, which would be approximately $2.8 \times 10^{14}$ elements for a $256^3$ Matrix.

The radial symmetry of the spectral shape $P(\vec{r},\vec{k})$ enables us to avoid a 3D correction with larger number of matrix elements and exceeding image reconstruction times. In the radial part of the sequence, half-spokes through $k$-space are acquired. These 1D lines can be processed with Eq. (11). Due to the radial symmetry, the inverted matrix $D_{kx}^{-1}$ has only to be calculated once during the entire reconstruction.

Using the Fourier slice theorem [15], the corrected image line $I(x) = f(x)$ could be processed in a three-dimensional projection- or Radon reconstruction [16]. The PETRA sequence consists of a radial and a Cartesian acquisition part. In order to correct and combine these two parts, we do not use a projection reconstruction, but Fourier transform the corrected line $I(x)$ back to $k$-space and apply a 3D gridding algorithm in $k$-space. This $k$-space line $F(k)$ is calculated from the corrected image $I(x)$ using the standard Fourier transformation given in Eq. (1). This equation can be written as a matrix equation with the matrix elements $E_{kx} = e^{ikx}$. Using Eq. (11), it can be found that the disturbed $k$-space $F'_k$ yields the undisturbed $k$-space $F_k$ as

$$F_k = E_{kx} D_{kx}^{-1} F'_k = C_{xk} F'_k. \tag{14}$$

Due to the radial symmetries, the matrix $C_{xk} = E_{kx} D_{kx}^{-1}$ also needs to be calculated only once during image reconstruction.

Because the amount of Cartesian points is not too large-about $N = 10$–$25$ points per line – the Cartesian part of the sequence is processed with the correction algorithm in 3D. As an example, for $N = 20$ points, $C_{xk}$ will have $N^6 = 6.4 \times 10^7$ complex points. This can be handled with current standard computer equipment.

The PETRA sequence can be extended to acquire a second gradient echo. A complete projection through $k$-space is acquired without any gap arising in the middle of $k$-space. The absolute gradient strength does not change during this projection so that Eq. (13) loses its dependency on $\vec{k}$. Due to the radial symmetries, Eq. (7) in this case describes a convolution and the disturbed image $I'(x)$ equals $I'(x) = f(x)P(x)$. For the second echo, the influence of the excitation profile can be either eliminated by division in image space or using Eq. (11) for the acquired radial projections.

### 3.3. Simulations

We used Eqs. (7) and (13) to simulate the disturbed $k$-space $F'(k)$ and image $I'(x)$ of a one-dimensional object $f(x)$, shown in Fig. 3. Using Eq. (11), the corrected image $I(x)$ was calculated from the disturbed $k$-space.

To be able to simulate 2D objects with $N > 60$, we used the radial symmetries of the problem as presented above. Starting from a 2D

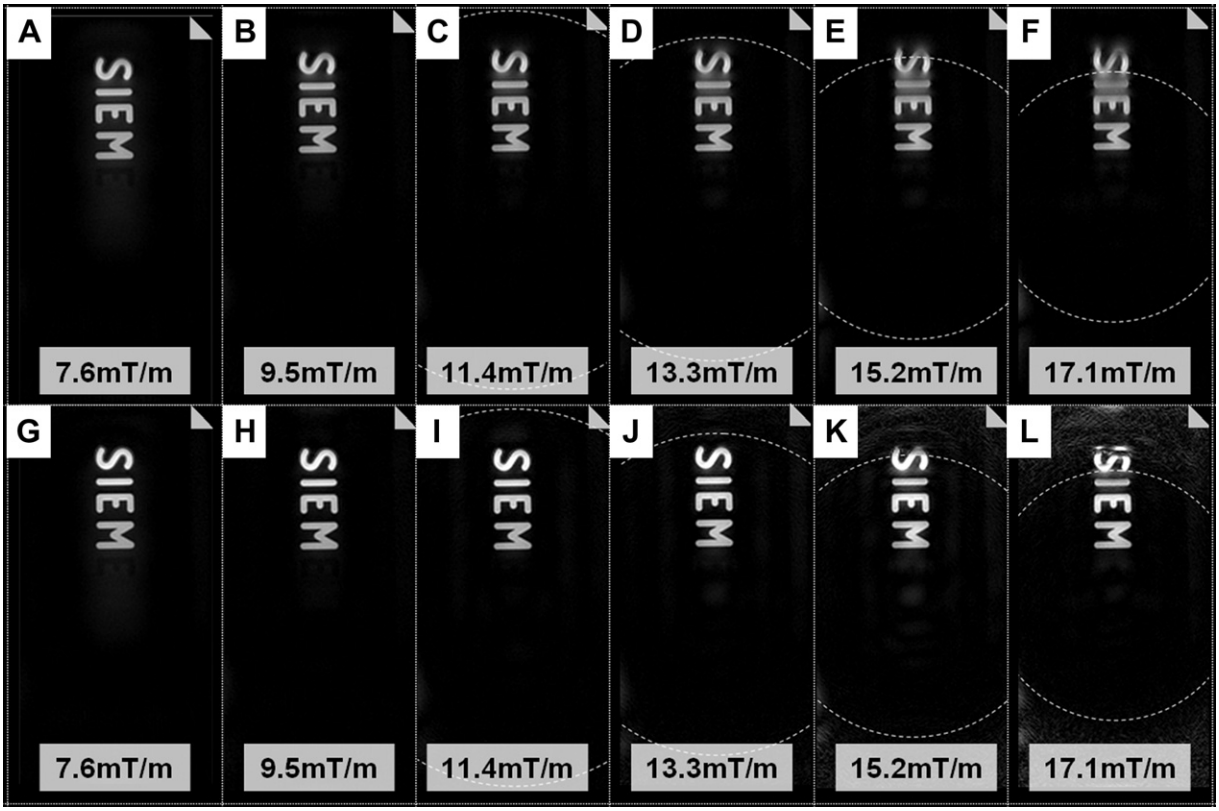


**Fig. 6.** Images of a structural phantom acquired with PETRA at different maximum gradient strengths without correction (A–F) and with correction (G–L). The dashed rings indicate $r_0$. Images have identical windowing scaled to the noise level. FOV was 300 mm isotropic, in vertical direction the complete FOV is shown.

object as shown in Fig. 4A, we first applied an inverse Radon transformation and then calculated the disturbed $k$-space line $F'(k)$ for each projection. Each of these lines was either Fourier back transformed for the disturbed image or processed with Eq. (11) for the corrected image. The images were calculated using a Radon transformation.

Simulations were performed using MATLAB 2008 (The MathWorks Inc, Natick, MA, USA). In all simulations, the pulse duration was set to $\tau = 14$ μs and different maximum gradient strengths (2–40 mT/m) were simulated for a simulated FOV of 300 mm, matrix size $N = 250$ and TE = 70 μs.

### 3.4. MR Measurements

The PETRA sequence was implemented and tested on a 3 T MAGNETOM Verio clinical scanner (SIEMENS Healthcare, Erlangen, Germany). Data post-processing and image reconstruction was implemented and performed in-line using the image calculation environment (ICE) of the scanner. The reconstruction is performed on a computer with 16 GB Ram and eight 2.83 GHz CPUs.

For all measurements we use a $\tau = 14$ μs hard pulse. In order to determine the actual pulse shape, the pulse was measured in a test scan with a TDS3034B oscilloscope (Tektronix Inc., Beaverton, OR, USA) that was connected to the radio frequency power amplifier (RFPA) of the scanner.

A structural phantom was imaged with different maximum gradient strengths of 7.6–17.1 mT/m. All other parameters were kept constant. The measurement was repeated with a phantom that contained fat and water in order to test the correction algorithm in the presence of chemical shift. In vivo head experiments were performed on healthy volunteers after informed consent and gradient strengths from 8.6 to 17.2 mT/m were used. The phantom and in vivo measurements were reconstructed with and without the application of the correction algorithm.

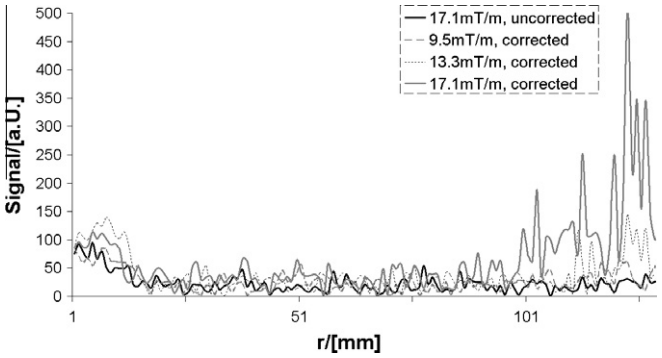


**Fig. 7.** Noise floor in images from the series shown in Fig. 6. A line pointing from the image center outwards was measured. Without correction, the noise floor is unchanged with increasing gradient strength. With correction, a radial increase of the noise levels is observed beyond the first minimum of the excitation $r_0$.

## 4. Results

The simulated one-dimensional object $f(x)$ with the calculated disturbed line $I'(x)$ are presented for different gradient strengths in Fig. 3. No differences are visible between the object $f(x)$ and the corrected image $I(x)$ (not shown in the figure). Simulations of the 2D object are presented in Fig. 4. Also here, no differences are detectable between the object $f(x,y)$ and the corrected image $I(x,y)$. For the 1D and 2D simulations, $P_{min}$ with the used settings equals 0.8 and 0.34 for 4 and 8 mT/m, $r_0$ equals 139.8, 104.9, 83.9, 55.9 and 41.9 mm for 12, 16, 20, 30 and 40 mT/m.

The measurement of the actual pulse shape showed minor differences between the optimal rectangular pulse p(t) and the actually pulse applied by the RFPA. The measured pulse has an exact duration of $\tau = 14$ μs with the spectral profile shown in Fig. 5. This

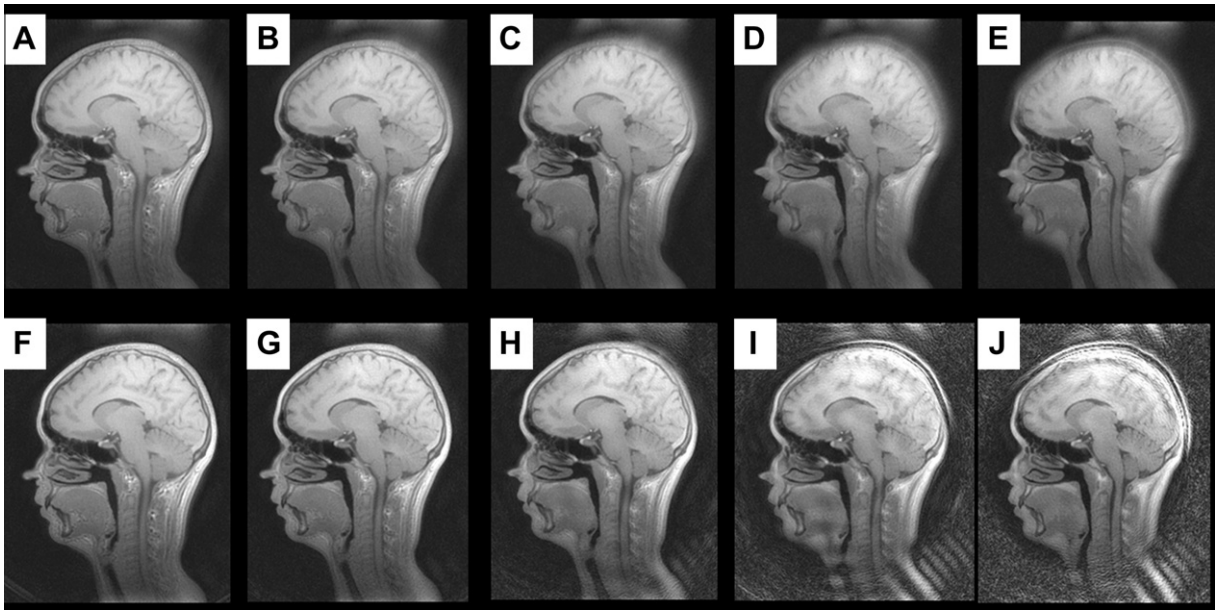


**Fig. 8.** In vivo head images acquired with PETRA at different maximum gradient strengths without correction (A–E) and with correction (F–J). Images have identical windowing. FOV was 300 mm isotropic, in vertical direction the complete FOV is shown. Gradients strengths were rising from 8.6 mT/m to 17.2 mT/m with steps of 2.15 mT/m.

measured profile was incorporated into the image correction algorithm.

Fig. 6 shows uncorrected and corrected structural phantom images with a FOV of 300 mm and different gradient strengths. For the measurement settings of the structural phantom, $P_{min}$ equals 0.39 and 0.17 for 7.6 and 9.5 mT/m, $r_0$ equals 147.2, 126.1, 110.4 and 98.1 mm for 11.4, 13.3, 15.2 and 17.1 mT/m. For 7.6 and 9.5 mT/m, $r_0$ is outside the FOV. Fig. 7 shows the noise floor measured in Fig. 6F, H, J and K on a line from image center outwards.

Original and corrected images of a phantom containing water and fat showed comparable results to the structural phantom. No artefacts arising during the correction due to chemical shift were detectable in the images.

Uncorrected and corrected in vivo head images obtained with different gradient strengths are presented in Fig. 8. $P_{min}$ with the used settings equals 0.27 and 0.04 for 8.6 and 10.75 mT/m, $r_0$ equals 130.0, 111.5 and 97.5 mm for 12.9, 15.05 and 17.2 mT/m. For 8.6 and 10.75 mT/m, $r_0$ is outside the FOV.

Image reconstruction times needed to reconstruct a dataset with an isotropic image matrix of $256^3$ takes about 0.5–1 min without correction and about 1.5 min with correction for one channel. Using four channels, image reconstruction times of about 1.5–2 min are needed without and 3–4 min with correction. Image reconstruction is performed in-line, so that also with applied correction the DICOM images are available a few seconds after the end of the scan.

## 5. Discussion

In ultrashort echo time sequences with non-zero gradients during the RF pulse, the excitation is not perfectly non-selective but a slice is excited. Throughout the sequence, this slice rotates and changes its thickness, as it is shown in Fig. 2. A homogeneous excitation is only achieved in $k$-space center while at the outer edges of $k$-space the image might not be excited sufficiently.

The 1D simulation presented in Fig. 3 shows the influence on the image for the PETRA sequence. Even at low gradient strengths, where the first minimum is far outside the FOV, intensity degradation is visible, see Fig. 3A. For stronger gradients, where the selected slice becomes smaller, severe blurring artefacts occur in the outer parts of the image. This can also be seen in the 2D PETRA simulation, see Fig. 4. The phantom and in vivo measurements show the same effect. Simulation and measurement are in almost perfect agreement. With smaller gradients, where the first minimum of the excitation is outside of the object, intensity errors in the outer parts as well as slight blurring are visible in both phantom and in vivo measurement, see Fig. 6A–F and Fig. 8A–E. Artefact-free imaging can be performed if $P_{min}$ is not smaller than 0.4, imaging with slight blurring at the edges of the FOV is still possible if $P_{min}$ is not smaller than 0.25. If $r_0$ lies within the object, radial blurring and ringing artefacts occur, as it can be seen in Fig. 4H, Fig. 6F and Fig. 8E. These artefacts are due to insufficient excitation of the outer image part at high $k$-space frequencies, while for lower $k$-space frequencies, the excitation is more homogeneous.

The proposed correction algorithm recovers the influence of the excitation pulse within the post-processing by matrix inversions in fast image reconstruction time. Using our correction approach, the influences of the spectral excitation profile can be completely eliminated in the simulation experiments. In the MR measurements, the functionality is proven, but limitations of the approach are found. If the first minimum of the excitation is outside of the object, the corrected images show an improved intensity homogeneity and the blurring is eliminated, see Fig. 6G, H and Fig. 8F, G. If the first minimum lies within the object, the algorithm is no longer able to recover the influences of the excitation outside of the minimum. The noise levels outside of the first minimum are raised as it is shown in Fig. 7 and the blurring cannot be recovered. As a limitation for the correction algorithm, $r_0$ should be outside of the object as the noise level is increased close to minimal excitations. This increase in noise level and signal folded into the image can also lead to the appearance of radial ringing artefacts, as it can be seen in Fig. 8J. Inside of $r_0$, an increased image quality is found and blurring is completely eliminated.

Using the correction, it is possible to use a broader frequency range and $P_{min}$ can be lowered from about 0.4–0.0 for the PETRA se-

quence. With this, higher readout bandwidths are enabled allowing shorter encoding times and less T2* blurring in ultrashort echo time imaging. Furthermore, longer pulses can be used that would allow for higher flip angles.

The correction algorithm presented here for the PETRA sequence can easily be adapted for other sequences with non-zero gradients during excitation like the ultrashort echo time sequences zTE, WASPI or RASP and SPRITE. It can also be used for non-selective sequences with non-zero gradients during excitation like the BURST sequence.

In conclusion, we have shown the influence of the excitation profile in hard pulse non-selective excitations in the presence of gradients and have presented an approach to eliminate artefacts in post-processing. Enhanced contrast is enabled and blurring can be eliminated. The limits of our approach have been investigated. Higher readout bandwidths or longer pulses with higher flip angles are enabled with our approach. This might help to establish this sequence class in clinical applications.

## References

[1] J. Hennig, M. Hodapp, Burst imaging, MAGMA 1 (1993) 39–48.
[2] O. Heid, M. Deimling, Rapid single point (RASP) imaging, in: Abstracts of the 3rd SMR Annual Meeting, 1995, pp. 684.
[3] B.J. Balcom, R.P. Macgregor, S.D. Beyea, D.P. Green, R.L. Armstrong, T.W. Bremner, Single-point ramped imaging with T1 enhancement (SPRITE), J. Magn. Reson. A 123 (1996) 131–134.
[4] M. Weiger, K.P. Pruessmann, F. Hennel, MRI with zero echo time: hard versus sweep pulse excitation, Magn. Reson. Med. 66 (2011) 379–389.
[5] S. Hafner, Fast imaging in liquids and solids with the back-projection low angle shot (BLAST) technique, Magn. Reson. Imag. 12 (1994) 1047–1051.
[6] Y. Wu, M.I. Hrovat, J.L. Ackerman, T.G. Reese, H. Cao, K. Ecklund, M.J. Glimcher, Bone matrix imaged in vivo by water- and fat-suppressed proton projection MRI (WASPI) of animal and human subjects, J. Magn. Reson. Imag. 31 (2010) 954–963.
[7] D.M. Grodzki, P.M. Jakob, B. Heismann, Ultrashort echo time imaging using pointwise encoding time reduction with radial acquisition (PETRA), Magn. Reson. Med. (2011).
[8] M.D. Robson, G.M. Bydder, Clinical ultrashort echo time imaging of bone and other connective tissues, NMR Biomed. 19 (2006) 765–780.
[9] G.H. Filho, J. Du, B.C. Pak, S. Statum, R. Znamorowski, P. Haghighi, G. Bydder, C.B. Chung, Quantitative characterization of the Achilles tendon in cadaveric specimens: T1 and T2* measurements using ultrashort-TE MRI at 3 T, AJR Am. J. Roentgenol. 192 (2009) W117–124.
[10] P.D. Gatehouse, R.W. Thomas, M.D. Robson, G. Hamilton, A.H. Herlihy, G.M. Bydder, Magnetic resonance imaging of the knee with ultrashort TE pulse sequences, Magn. Reson. Imag. 22 (2004) 1061–1067.
[11] A.K. Bracher, C. Hofmann, A. Bornstedt, S. Boujraf, E. Hell, J. Ulrici, A. Spahr, B. Haller, V. Rasche, Feasibility of ultra-short echo time (UTE) magnetic resonance imaging for identification of carious lesions, Magn. Reson. Med. 66 (2011) 538–545.
[12] D.J. Tyler, M.D. Robson, R.M. Henkelman, I.R. Young, G.M. Bydder, Magnetic resonance imaging with ultrashort TE (UTE) PULSE sequences: technical considerations, J. Magn. Reson. Imag. 25 (2007) 279–289.
[13] D.O. Kuethe, A. Caprihan, I.J. Lowe, D.P. Madio, H.M. Gach, Transforming NMR data despite missing points, J. Magn. Reson. 139 (1999) 18–25.
[14] D. Idiyatullin, C. Corum, J.Y. Park, M. Garwood, Fast and quiet MRI using a swept radiofrequency, J. Magn. Reson. 181 (2006) 342–349.
[15] A.C. Kak, M. Slaney, Principles of computerized tomographic imaging, Society of Industrial and Applied Mathematics, 2001.
[16] J.S. Lim, Two-Dimensional Signal and Image Processing, Prentice Hall, Englewood Cliffs, NJ, 1990. 42–45.